Guidelines to Classical Frequency-Domain Disturbance Observer Redesign for Enhanced Rejection of Periodic Uncertainties and Disturbances

Moria Elkayam, *Student Member, IEEE*, Sergei Kolesnik, *Student Member, IEEE*, and Alon Kuperman, *Senior Member, IEEE*

***Abstract*—The paper suggests a method aimed to improve the performance of dynamical systems with periodic uncertainties and disturbances (ac power converters are typical representatives of such systems) utilizing frequency-domain disturbance observer (DOB)-based control structure. In such control arrangement, DOB filter is the key component and should be designed so that its magnitude (phase) is as close to unity (zero) as possible at frequencies where the total uncertainty and disturbance exists. The methodology for designing DOB filters is well established mostly for systems with slow-varying uncertainties/disturbances and has been barely extended to systems with periodic excitation (such as grid-connected or stand-alone ac power converters). In this study, systematic enhancement of DOB filters, designed according to the classical methodology, is suggested based on appropriate mixing with a series multiresonant term. The proposed approach allows attaining improved periodic signals rejection capability while significantly sacrificing neither the dc gain nor the crossover frequency. Quantitative design guidelines are provided, and possible tradeoffs are revealed. The proposed methodology is validated by application to current control of *LCL*-filter-based inverter connected to a distorted ac grid. Feasibility and performance of the suggested approach are well supported by simulations and experiments.**

***Index Terms*—Disturbance observer (DOB), periodic uncertainty and disturbance, multiresonant term.**

I. Introduction

UNCERTAINTIES and disturbances (imposed by parameter variations and/or unmodeled dynamics) commonly exist in industrial systems, bringing adverse effects into closed-loop control performance and stability [1]. Not surprisingly, uncertainty and disturbance rejection is therefore one of the key objectives in a typical industrial control system design.

Manuscript received January 4, 2018; revised April 9, 2018; accepted July 31, 2018. Date of publication August 14, 2018; date of current version February 20, 2019. Recommended for publication by Associate Editor J. A. Oliver. *(Corresponding author: Alon Kuperman.)*

M. Elkayam is with the Department of Electrical Engineering and Electronics, Ariel University of Samaria, Ariel 40700, Israel (e-mail:

frequency-domain DOB to cope with non-dc uncertainties and disturbances as well. Therefore, this paper proposes a methodology of enhancing any frequency-domain DOB, designed according to classical methods. The proposed idea is inspired by recent work in [26], stating that it is possible to design a DOB for any type of uncertainty and disturbance by embedding a suitable internal model. Following the line of thinking, this study proposes a frequency-domain DOB, based on a classical *Q*-filter appropriately mixed with a multiresonant term, allowing proper estimation and subsequent elimination of periodic uncertainties and disturbances. Unlike other works, utilizing a multiresonant control structure, consisting of parallel connection of single resonant terms [27], [28], a series connected structure is proposed here, which is more simple and straightforward.

The proposed methodology is then applied to current control of a grid-connected *LCL* inverter. It is well known that injection of low-harmonic current to the grid is regulated by international standards. In order to accomplish these standards, precise current control is required in order to comply with the power-quality requirements and assure accurate active and reactive power interchange despite possible parameter uncertainties and distorted grid [29]. In grid-connected inverters, selective harmonic compensation is carried out by means of resonant harmonic compensators [30], yielding satisfactory results. Nevertheless, single-degree-of-freedom control structures are typically utilized. As a result, disturbance rejection and tracking problems are coupled [31]. DOB-based approach possesses two-degree-of-freedom structure, allowing to decouple disturbance rejection and tracking challenges by nearly independent design of DOB and nominal tracking controller [32]. Another advantage addressed by the proposed control structure is the possibility of the ac voltage sensorless operation, which has been addressed in several *LCL*-inverter-related recent works [33]–[36], in which advanced control theory algorithms (namely artificial neural networks and extended state observers) were used to estimate ac-side voltages. The approach proposed in the paper allows relatively simple design of an observer, which considers ac voltage as part of lumped disturbance and is capable of accurately estimating it along with associated parameter uncertainties.

The rest of the paper is organized as follows. The problem of rejecting periodic uncertainties and disturbances using classical DOB is briefly reviewed in Section II. The proposed solution is revealed and analyzed in Section III. Design guidelines are given in Section IV, taking practical issues into account. An example of applying the proposed methodology to current control of *LCL* inverter, connected to distorted ac grid, is provided in Section V and is validated by simulations and experiments in Section VI. The paper is concluded in Section VII.

II. General Problem Formulation

Consider an uncertain system with disturbance, described by the following input–output relation:

$$y(s)=\underbrace{(P_n(s)+\Delta P(s))}_{P(s)}(u(s)+w(s))=P_n(s)\,(u(s)+d(s)) \tag{1}$$

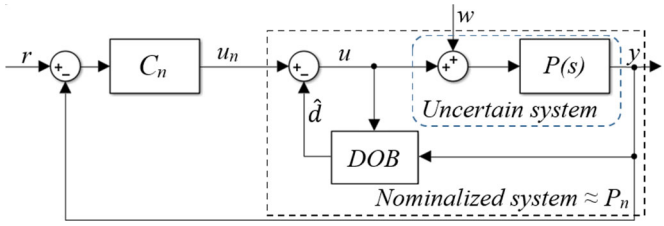

Fig. 1. General DOB-based control structure.

with $u(s)$ and $y(s)$ denoting the control input and the system output, respectively, $w(s)$ symbolizing the unmeasurable external disturbance, $P_n(s)$ and $\delta P(s)$ representing the corresponding known and uncertain parts of the stable minimum-phase plant $P(s)$, and

$$d(s)=P_n^{-1}(s)\Delta P(s)u(s)+\left(1+P_n^{-1}(s)\Delta P(s)\right)w(s) \tag{2}$$

signifying the lumped uncertainty and disturbance (LUD). In frequency-domain DOB-based control structures, the control input is typically split as

$$u(s)=u_n(s)-\hat{d}(s) \tag{3}$$

where $u_n(s)$ represents the output of a nominal tracking controller C_n (designed according to $P_n(s)$) and $\hat{d}(s)$ denotes the DOB-generated LUD estimate, as shown in Fig. 1. In case $\hat{d}(s)\approx d(s)$, (1) reduces to

$$y(s)=P_n(s)u_n(s) \tag{4}$$

and is referred to as "nominalized" system.

In order to create a suitable LUD estimate, note that according to (1)

$$d(s)=y(s)P_n^{-1}(s)-u(s). \tag{5}$$

Apparently, (5) cannot be used as is due to causality issues. Typical frequency-domain DOB estimates the LUD by passing (5) through a filter $G(s)$ as

$$\hat{d}(s)=d(s)G(s)=\left(y(s)P_n^{-1}(s)-u(s)\right)G(s) \tag{6}$$

i.e., unknown uncertainties and disturbances are estimated from known parameters and measured signals only. Combining (6) with (3) and rearranging yields

$$\hat{d}(s)=\frac{G(s)}{1-G(s)}\left(y(s)P_n^{-1}(s)-u_n(s)\right). \tag{7}$$

The inner loop gain and sensitivity functions are then given by

$$\mathrm{LG}_{\mathrm{DOB}}(s)=\frac{G(s)}{1-G(s)},\quad H(s)=1-G(s) \tag{8}$$

respectively. Substituting (7) into (1), we get

$$y(s)=P_n(s)\left(u_n(s)+(1-G(s))d(s)\right) \tag{9}$$

as shown in Fig. 2. It is interesting to note that despite the fact that $d(t)$ in nonmeasurable, utilizing frequency-domain DOB-based structure allows achieving effect of passing $d(t)$ through

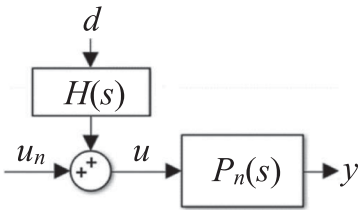

Fig. 2. Equivalent simplified block diagram inner closed loop.

a filter $H(s) = 1 - G(s)$ without actually accessing it. Moreover, according to (9), nominal controller output $u_n(s)$ remains unaffected by the DOB.

Observing (9), it is obviously desired to have $G(s) = 1$ at frequencies where $d(s) \neq 0$ in order to achieve perfect system nominalization. In frequency-domain DOB-related literature, a low-pass filter

$$G(s) = \frac{1 + \sum_{n=1}^{N} b_n s^n}{1 + \sum_{m=1}^{M} a_m s^m} \tag{10a}$$

giving

$$H(s) = 1 - G(s) = \frac{\sum_{m=1}^{M} a_m s^m - \sum_{n=1}^{N} b_n s^n}{1 + \sum_{m=1}^{M} a_m s^m} \tag{10b}$$

with $M > N$ is typically utilized, i.e., $|H(j\omega)| = 0$ for $\omega = 0$ and $|H(j\omega)| > 0$ for $\omega > 0$. In case $|d(j\omega)| \neq 0$ for $\omega > 0$, respective contents of $\hat{d}(s)$ are only an approximation of the corresponding $d(s)$ constituents. Moreover, the estimation error obviously increases with the increase in ω since the magnitude of $H(s)$ decreases, depending on both available control bandwidth [or equivalently the maximum attainable bandwidth of $G(s)$] and filter order. Hence, in case (10) is utilized, estimation quality may only be enhanced by increasing either the filter order (which in turn decreases stability) or the control bandwidth [37]. Taking (10) into account, inner loop gain becomes

$$\mathrm{LG}_{\mathrm{DOB}}(s) = \frac{\sum_{n=1}^{N} b_n s^n + 1}{\sum_{m=1}^{M} a_m s^m - \sum_{n=1}^{N} b_n s^n} \tag{11}$$

characterized by infinite gain at dc only.

In case the LUD in (2) possesses periodic behavior, it is given in time domain by

$$d(t) = \sum_{k=J}^{K} D_k \sin\left(k\omega_0 t + \varphi_n\right) \tag{12}$$

with ω_0 symbolizing base operating frequency and *J, K* denoting the order of the lowest and highest harmonic possessing significant energy, respectively. In reality, energy content of (12) is concentrated at multiples of ω_0 so that $D_{k+1} < D_k \; \forall k$. In case $G(s)$ in (10) is utilized, the magnitude of corresponding $H(s)$ is zero at dc and rises with the increase in k. In general, magnitude of LUD estimation error is given by

$$|e_d(jk\omega_0)| = \left|d(jk\omega_0) - \hat{d}(jk\omega_0)\right| = D_k \left|H(jk\omega_0)\right|. \tag{13}$$

Note that low-frequency uncertainty and/or disturbance always exists in practical systems; hence, zero magnitude of $H(s)$ at dc is a desirable feature. Moreover, the higher the available control bandwidth, the faster are the transients. Hence, the bandwidth of $G(s)$ should always be selected as high as possible to speed up the transients. The main deficiency of $G(s)$ in (10) is hence the nonunity gain and nonzero phase at multiples of ω_0. It is therefore desired to modify the classical frequency-domain DOB filter so that

$$G_m(s) = \begin{cases} 1, & \omega = k\omega_0 \\ G(s), & \text{elsewhere} \end{cases} \tag{14a}$$

i.e.,

$$H_m(s) = 1 - G_m(s) = \begin{cases} 0, & \omega = k\omega_0 \\ H(s), & \text{elsewhere} \end{cases} \tag{14b}$$

giving

$$|e_d(jk\omega_0)| = D_k \left|H_m(jk\omega_0)\right| = 0, \qquad k = 1, 2, 3 \ldots \tag{15}$$

This allows preserving the dc gain and crossover frequency of classical frequency-domain DOB while significantly enhancing its disturbance rejection capabilities at multiples of ω_0.

III. Proposed Methodology

Consider a typical resonant term [27], given by

$$\mathrm{HR}_k(s) = \frac{2a_k s}{s^2 + (k\omega_0)^2} \tag{16}$$

with

$$\begin{aligned} |\mathrm{HR}_k(j\omega)| &\approx \begin{cases} \infty, & \omega = k\omega_0 \\ 0, & \text{elsewhere} \end{cases} \\ \angle \mathrm{HR}_k(j\omega) &\approx \begin{cases} 90^\circ, & 0 \leq \omega < k\omega_0 \\ -90^\circ, & \omega > k\omega_0. \end{cases} \end{aligned} \tag{17}$$

Define a reformed resonant term as

$$R_k(s) = 1 + \mathrm{HR}_k(s) = 1 + \frac{2a_k s}{s^2 + (k\omega_0)^2} = \frac{s^2 + 2a_k s + (k\omega_0)^2}{s^2 + (k\omega_0)^2} \tag{18}$$

with

$$\begin{aligned} |R_k(j\omega)| &= \begin{cases} \infty, & \omega = k\omega_0 \\ \sqrt{2}, & \omega = k\omega_0 \pm a_k \\ 1, & \omega << k\omega_0 - a_k \\ & \omega >> k\omega_0 + a_k \end{cases} \\ \angle R_k(j\omega) &= \begin{cases} \pm 90^\circ, & \omega \to (k\omega_0)^{\mp} \\ \pm 45^\circ, & k\omega_0 \mp a_k \\ 0, & \omega << k\omega_0 - a_k \\ & \omega >> k\omega_0 + a_k. \end{cases} \end{aligned} \tag{19}$$

Corresponding Bode diagrams are shown in Fig. 3. In order to realize (14), it is proposed to modify the classical frequency-domain DOB filter by an expression, consisting of multiple

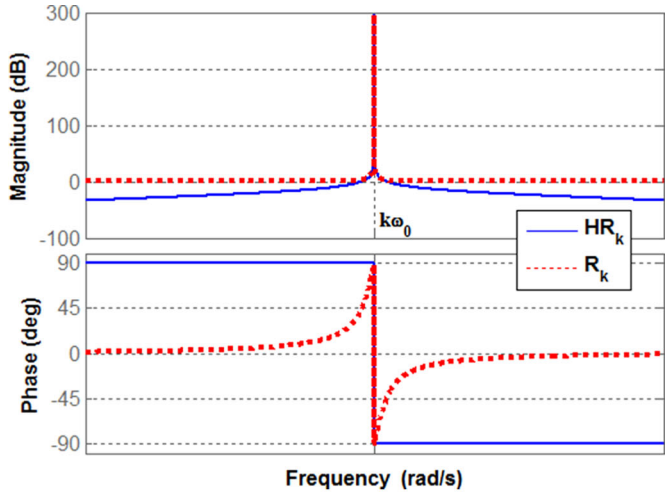

(a)

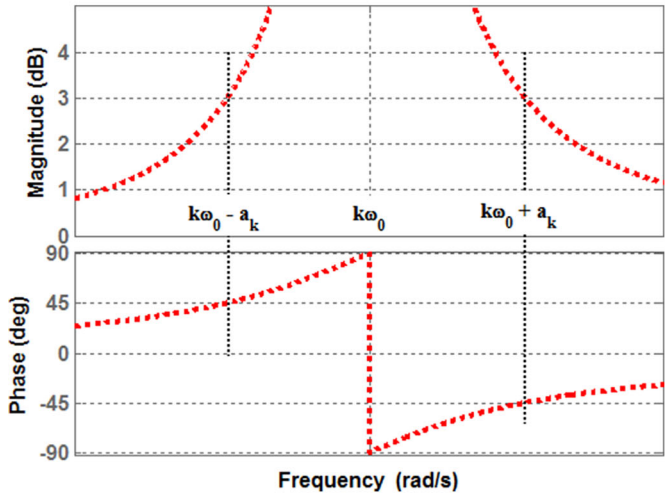

(b)

Fig. 3. Frequency-domain representation of resonant terms. (a) Bode diagrams of $R_k(s)$ and $HR_k(s)$. (b) Zoomed view of $R_k(s)$.

series-connected reformed resonant terms

$$R(s)=\prod_{k=J}^{K}R_k(s)=\prod_{k=J}^{K}\left(1+\frac{2\alpha_k s}{s^2+(k\omega_0)^2}\right) \tag{20}$$

so that

$$G_R(s)=\frac{\sum_{n=1}^{N}b_n s^n+R(s)}{\sum_{m=1}^{M}a_m s^m+R(s)} \approx \begin{cases} 1, & \omega=k\omega_0 \\ \underbrace{\dfrac{\sum_{n=1}^{N}b_n s^n+1}{\sum_{m=1}^{M}a_m s^m+1}}_{G(s)}, & \text{elsewhere} \end{cases} \tag{21}$$

obviously satisfying (12). Bode diagram of $R(s)$ is depicted in Fig. 4. Note that for frequencies much lower than $J\omega_0$ and much higher than $K\omega_0$, the series-connected multiresonant term is unity. Taking (21) into account, the inner loop gain is

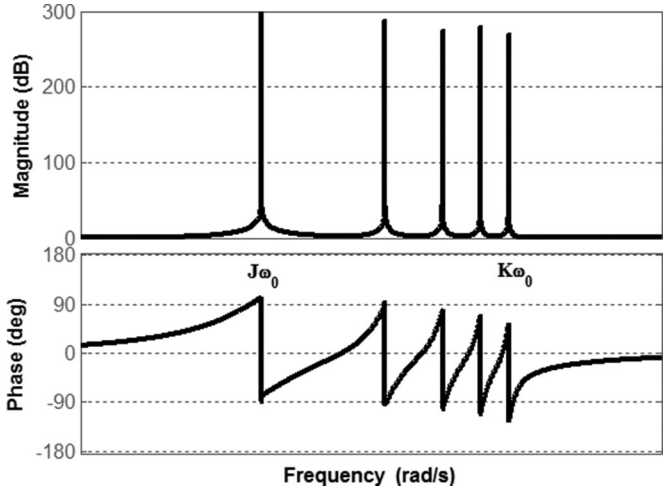

Fig. 4. Bode diagram of series-connected multiresonant term.

given by

$$\mathrm{LG}_{\mathrm{DOB},R}(s)=\frac{\sum_{n=1}^{N}b_n s^n+R(s)}{\sum_{m=1}^{M}a_m s^m-\sum_{n=1}^{N}b_n s^n} \approx \begin{cases} \infty, & \omega=k\omega_0 \\ \underbrace{\dfrac{\sum_{n=1}^{N}b_n s^n+1}{\sum_{m=1}^{M}a_m s^m-\sum_{n=1}^{N}b_n s^n}}_{\mathrm{LG}_{\mathrm{DOB}}(s)}, & \text{elsewhere} \end{cases} \tag{22}$$

possessing infinite gain at dc and multiples of ω_0, as desired.

IV. Practical Issues and Design Guidelines

In practice, a typical resonant term (16) is usually modified as

$$\mathrm{HR}_{km}(s)=\frac{2a_k s}{s^2+2b_k s+(k\omega_0)^2} \tag{23}$$

with $0<b_k<<a_k$ to improve robustness of base frequency variations and finite word length (in case of digital implementation) while maintaining high resonant gain [28]. Then, (18) and (20) become

$$R_{km}(s)=\frac{s^2+2(a_k+b_k)s+(k\omega_0)^2}{s^2+2b_k s+(k\omega_0)^2} \tag{24}$$

and

$$R_m(s)=\prod_{k=J}^{K}R_{km}(s) \tag{25}$$

respectively, with

$$|R_{km}(jk\omega_0)|=1+\frac{a_k}{b_k}, \qquad \left|\angle R_k(\omega\to(k\omega_0)^{\mp})\right|<90^\circ. \tag{26}$$

In order to emphasize the influence of a_k and b_k on the frequency response of resonant terms, Fig. 5(a) demonstrates the

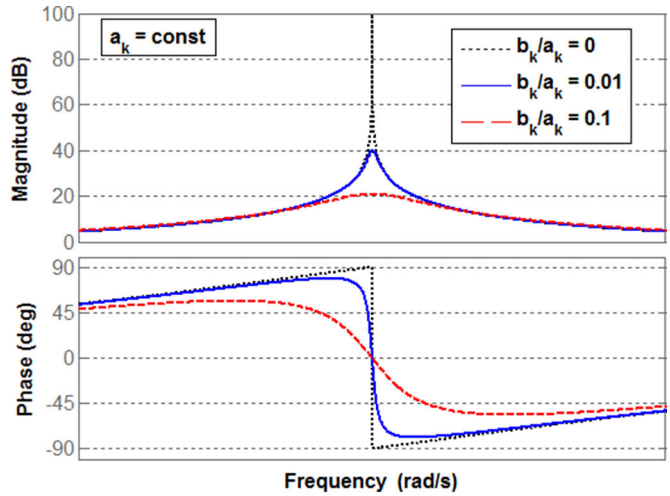

(a)

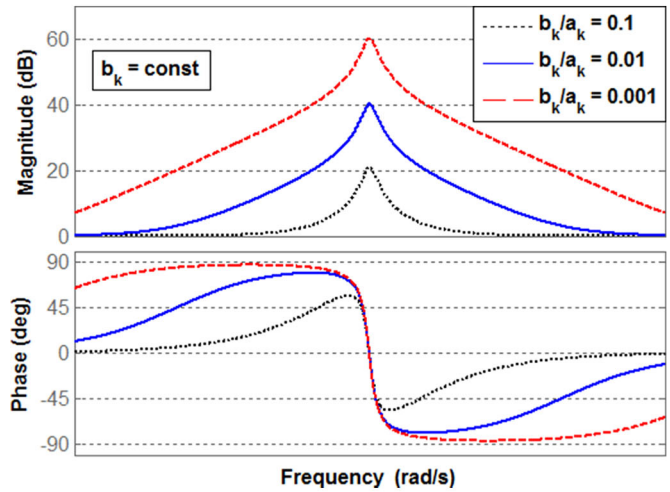

(b)

Fig. 5. Influence of a_k and b_k on the frequency response of resonant terms. (a) b_k variation for a given a_k. (b) a_k variation for a given b_k.

variation of the latter upon increase of b_k for a given a_k. Apparently, along with the bandwidth increase (and thus robustness improvement to base frequency variations) and less abrupt phase change, resonant gain decreases. On the other hand, Fig. 5(b) demonstrates the influence of increasing a_k for a given nonzero b_k. It may be concluded that while the bandwidth remains unchanged, resonant gain rises and the frequency range of phase influence increases as well. In case the crossover frequency is higher than the resonant frequency, nonzero gain and negative phase are expected to reduce system stability, imposing a clear tradeoff.

Utilizing (25), the modified DOB filter is given by

$$G_m(s) = \frac{\sum_{n=1}^{N} b_n s^n + R_m(s)}{\sum_{m=1}^{M} a_m s^m + R_m(s)}. \tag{27}$$

Furthermore, in practical systems $T_a(s)$ should be properly taken into account. The inner loop gain and the corresponding sensitivity function are then expressed by

$$\mathrm{LG}_{\mathrm{DOB},m}(s) = \frac{\sum_{n=1}^{N} b_n s^n + R_m(s)}{\sum_{m=1}^{M} a_m s^m - \sum_{n=1}^{N} b_n s^n} T_a(s)$$
$$H_m(s) = \frac{1}{1 + \mathrm{LG}_{\mathrm{DOB},m}(s)}. \tag{28}$$

Note that $|\mathrm{LG}_{\mathrm{DOB},m}(jk\omega_0)| >> 1$, then $|H_m(jk\omega_0)| \approx |\mathrm{LG}_{\mathrm{DOB},m}(jk\omega_0)|^{-1}$. Thus, the following design guidelines may be established:

1) Identify $T_a(s)$.
2) Set a desired phase margin φ_M.
3) Select $G(s)$ so that $LG(s)\cdot T_a(s)$ satisfies φ_M. Denote the resulting crossover frequency as $\omega_{C\max}$, which serves as the upper bound for achievable bandwidth.

At this point, priority of the following performance merits should be determined: transients decay rate (corresponding to the loop gain crossover frequency), steady-state error (corresponding to the loop gain resonant peak values), and robustness to base frequency variations (corresponding to the loop gain resonant peak bandwidths). Once the most valuable merit is set, the other two are subject to tradeoff. In the following, control bandwidth is selected as the highest priority performance merit and robustness to base frequency variations is chosen as the lowest priority performance merit.

4) Select the target crossover frequency $\omega_C \le \omega_{C\max}$. This imposes

$$|\mathrm{LG}_{\mathrm{DOB},m}(j\omega_C)| = 1,$$
$$\angle \mathrm{LG}_{\mathrm{DOB},m}(j\omega_C) = -180^\circ + \varphi_M. \tag{29}$$

5) Set the desired values of sensitivity function magnitude at resonant frequencies

$$|H_m(jk\omega_0)| \cong |\mathrm{LG}_{\mathrm{DOB},m}(jk\omega_0)|^{-1} = G_k^{-1}$$
$$k = J, .., K. \tag{30}$$

It is assumed (without loss of generality) that the filter has a predetermined structure, where all the coefficients are known functions of a single parameter (e.g., Butterworth). Therefore, $\mathrm{LG}_{\mathrm{DOB},m}$ is defined by $2(K-J)+3$ parameters. On the other hand, (29) and (30) form $K-J+3$ independent equations. Hence, only $K-J$ independent equations are required to form a full equations system. Therefore, only $K-J$ out of $K-J+1$ values of resonant peak bandwidths may be independently set.

6) Set the preferred values of resonant peak bandwidths so that

$$|\mathrm{LG}_{\mathrm{DOB},m}(j\gamma_k k\omega_0)| = \frac{G_k}{\sqrt{2}}, \qquad k = J, .., K, \qquad k \neq n \tag{31}$$

with $\gamma_k > 1$, i.e., nth resonant peak bandwidth will be design outcome rather than requirement.

7) Solve (29)–(31) using any available computational software package. In case a solution cannot be attained, release one (or more) requirement(s) and repeat until succeeded.

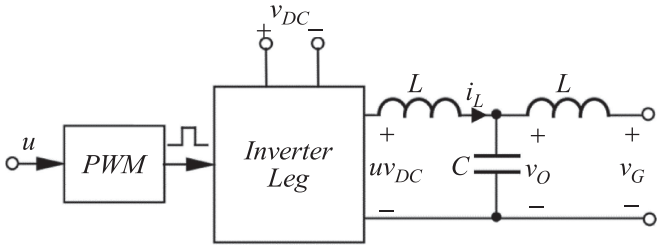

Fig. 6. Typical single-phase *LCL*-filter-based inverter.

TABLE I
NOMINAL SYSTEM PARAMETER VALUES

Parameter	Value	Units
Switching frequency	20	*kHz*
Sampling frequency	20	*kHz*
Inductance, *L*	3.5	*mH*
Inductor ESR, *R*	10	*mΩ*
Capacitance, *C*	1	*μF*
Base frequency	50	*Hz*

V. APPLICATION TO CURRENT CONTROL OF A DISTORTED-GRID-CONNECTED *LCL* INVERTER

Consider a grid-connected inverter shown in Fig. 6, consisting of a single-phase *LCL*-filter-terminated leg, powered by a dc source $v_{\rm dc}$. The control signal u is converted to a pulsewidth-modulated (PWM) signal, driving the converter. The inverter is connected to a distorted grid v_G given by

$$v_G(t) = \sum_{k=1,3,5} V_k \sin\,(k\omega_0 t)\ (\mathrm{V}). \tag{32}$$

Numerical values of other relevant system parameters are summarized in Table I. Inverter current dynamics may be described by the following switching-period-averaged equation:

$$\begin{aligned}\frac{di_L(t)}{dt} &= \underbrace{(L_n^{-1}+\Delta L^{-1})}_{L^{-1}}(u(t)\underbrace{(V_{\rm dc}+\Delta v_{\rm dc})}_{v_{\rm dc}} - Ri_L(t) - v_O(t)) \\ &= V_{\rm dc}L_n^{-1}\,(u(t)+d(t))\end{aligned} \tag{33}$$

with *R* denoting inductor ESR, assumed unknown. In case the inductor current satisfies

$$i_L(t) = \sum_{k=1,3,5} I_{Lk} \sin\,(k\omega_0 t + \theta_k) \tag{34}$$

inverter output voltage is given by

$$v_O(t) = \sum_{k=1,3,5} \frac{V_k \sin\,(k\omega_0 t) + I_{Lk} k\omega_0 L \cos\,(k\omega_0 t + \theta_k)}{1-(k\omega_0)^2 LC}. \tag{35}$$

Referring to (1)

$$\begin{aligned}P_n(s) &= \tfrac{V_{\rm dc}L_n^{-1}}{s} \\ d(t) &= \tfrac{L_n}{V_{\rm dc}}\left(\left(\Delta L^{-1}v_{\rm dc} + L_n^{-1}\Delta v_{\rm dc}\right)u(t) - \tfrac{Ri_L(t)+v_O(t)}{L}\right).\end{aligned} \tag{36}$$

TABLE II
DESIGN OUTCOMES—PARAMETER VALUES

Parameter	ω_{Cm}	a_1	a_2	a_3	b_1	b_2	b_3
Value	2000π	750	125	100	3.2	9.5	15.8

The resulting LUD term is obviously well described by (12). The overall sampling and switching delay is selected as 1.5 times the switching period [38], i.e.,

$$T_a(s) = e^{-\frac{1.5}{20000}s}. \tag{37}$$

Without loss of generality, a first-order Butterworth filter is typically utilized in DOB-based controllers

$$G(s) = \frac{1}{\omega_C^{-1}s+1} \tag{38}$$

is considered. Then

$$\mathrm{LG}(s) = \tfrac{\omega_C}{s}, \quad H(s) = \tfrac{s}{s+\omega_C}. \tag{39}$$

Setting a desired value of phase margin to $\varphi_M = 45^\circ$ results in $\omega_{\mathrm{C}\max} = 10\ 000\pi/3$ rad/s (see [38] for detailed derivation guidelines). Next, $G(s)$ is modified as

$$G_m(s) = \frac{\prod_{k=1}^{3}\left(\frac{s^2+2(a_k+b_k)s+(k\omega_0)^2}{s^2+2b_k s+(k\omega_0)^2}\right)}{\omega_{Cm}^{-1}s + \prod_{k=1}^{3}\left(\frac{s^2+2(a_k+b_k)s+(k\omega_0)^2}{s^2+2b_k s+(k\omega_0)^2}\right)} \tag{40}$$

giving

$$\mathrm{LG}_{\mathrm{DOB},m}(s) = \frac{e^{-\frac{1}{20000}s}}{\omega_{Cm}^{-1}s}\prod_{k=1}^{3}\left(\frac{s^2+2(a_k+b_k)s+(k\omega_0)^2}{s^2+2b_k s+(k\omega_0)^2}\right). \tag{41}$$

Since $J=1$ and $K=3$, the modified loop gain is described by seven parameters. The target crossover frequency is chosen as $\omega_{\mathrm{C}} = 2000\pi$ rad/s $< \omega_{\mathrm{C}\max}$. The desired values of sensitivity function magnitude at resonant frequencies are set to

$$\begin{aligned}|H_m(jk\omega_0)| &\cong |\mathrm{LG}_{\mathrm{DOB},m}(jk\omega_0)|^{-1} \\ &= \begin{cases} 4800^{-1}(-73.6\ \mathrm{dB}), & k=1 \\ 200^{-1}(-46\ \mathrm{dB}), & k=3 \\ 45^{-1}(-33.1\ \mathrm{dB}), & k=5. \end{cases}\end{aligned} \tag{42}$$

Lastly, the preferred values of resonant peak bandwidths of the first and third harmonics are selected so that

$$\gamma_k = 1.01, \quad k=1,3. \tag{43}$$

A system of seven equations with seven unknowns is then solved, yielding parameter values summarized in Table II. Bode diagrams, comparing the loop gains and sensitivity functions corresponding to $G(s)$ and $G_m(s)$, are shown in Fig. 7.

It may be concluded that DOB equipped with modified filter outperforms the classical at the vicinity of resonant frequencies, as expected. On the other hand, the sensitivity function of the latter possesses higher attenuation at high frequencies (above 600π rad/s) due to higher crossover frequency, as expected from the Bode integral theorem ("waterbed" effect). Bode diagram of the modified sensitivity function magnitude zoomed around

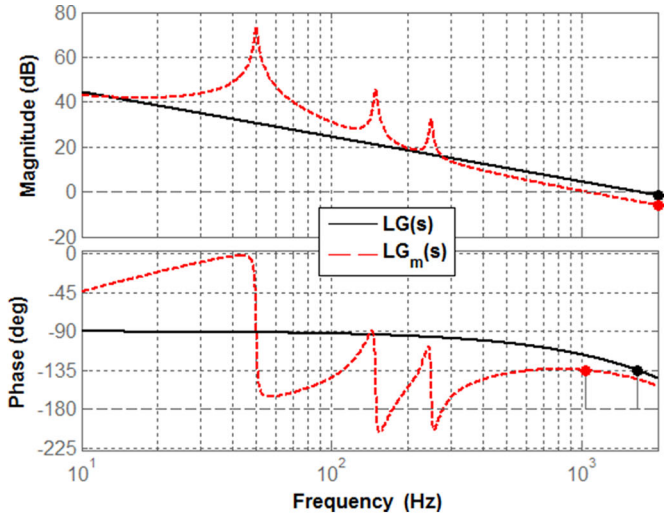

(a)

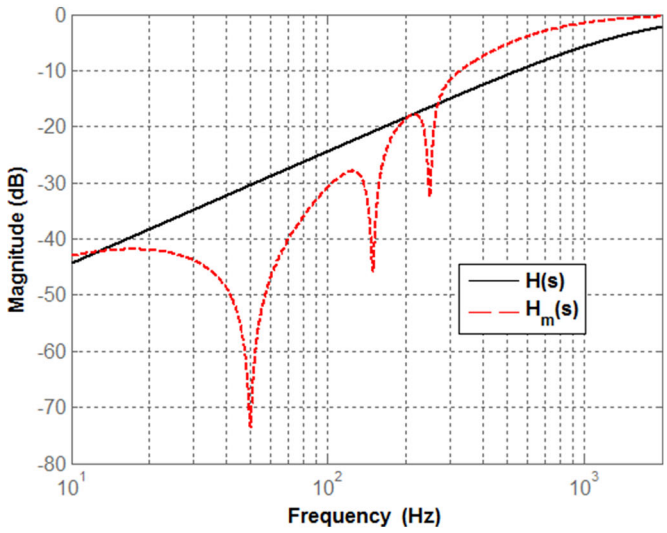

(b)

Fig. 7. Performance comparison of the classical and modified DOBs by means of Bode diagrams. (a) Loop gains. (b) Sensitivity function magnitudes.

resonant frequencies is shown in Fig. 8, verifying compliance with design requirements in (40) and (41). Furthermore, it is interesting to note the design yields the third resonant peak bandwidth value similar to the designed ones, i.e., $\gamma_3 \approx 1.01$.

VI. Verification

In order to verify the time-domain performance of the proposed algorithm and compare it to the classical one, simulations and experimental studies were carried out, based on the system in Fig. 6 with circuit parameters, controller parameters, and voltage values given in Tables I–III, respectively.

A. Simulations

Simulations were performed using PSIM software. The nominal controller output u_n (cf. Fig. 1) was set to zero and $\hat{d}$ was estimated and counteracted by DOB utilizing filters in (36) and (38). The results are shown in Figs. 9–11.

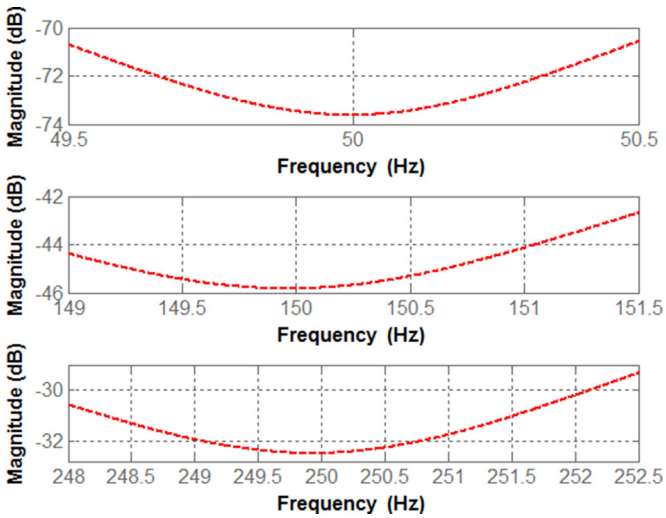

Fig. 8. Magnitude of sensitivity function $H_m(s)$ zoomed around resonant frequencies.

TABLE III
Voltage Values Adopted for Verification

Parameter	Simulation	Experiment
v_{DC} [V]	400	50
V_1 [V]	325	40.625
V_3 [V]	50	6.25
V_5 [V]	20	2.5

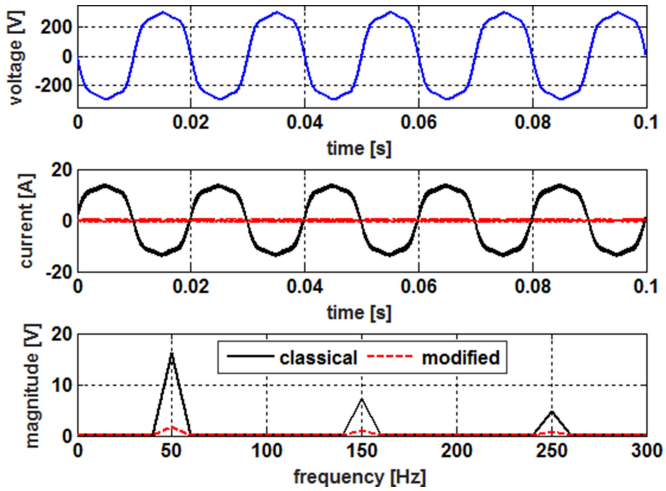

Fig. 9. Simulation results: grid voltage (top) and inductor currents in time (middle) and frequency (bottom) domains.

Fig. 9 presents the time-domain plots of the distorted grid voltage and inductor currents for both DOBs and frequency-domain magnitudes of the latter. Apparently, while significant steady-state error is present when original DOB is utilized, the LUD is almost fully rejected by the modified one. Fig. 10 demonstrates the nearly seamless operation transition from original to modified DOB-based controllers at $t = 0.1$ s, verifying fast transients decay. Fig. 11 presents the modified DOB-controller-based system response to 15% step-like variations of grid voltage. It may

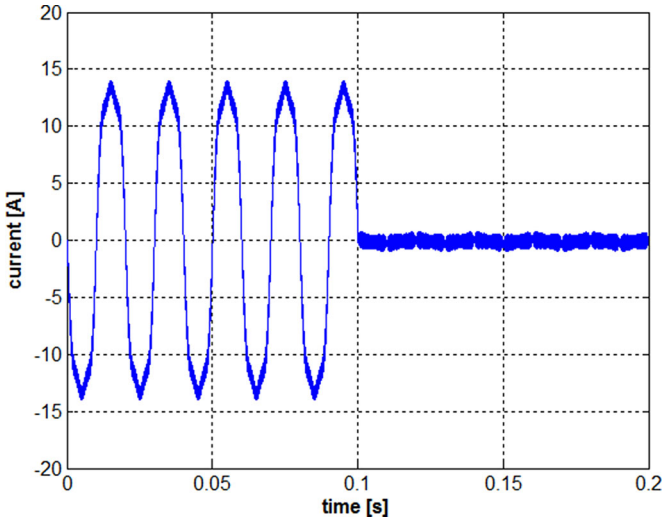

Fig. 10. Simulation results. Classical-to-modified DOB-based operation transition.

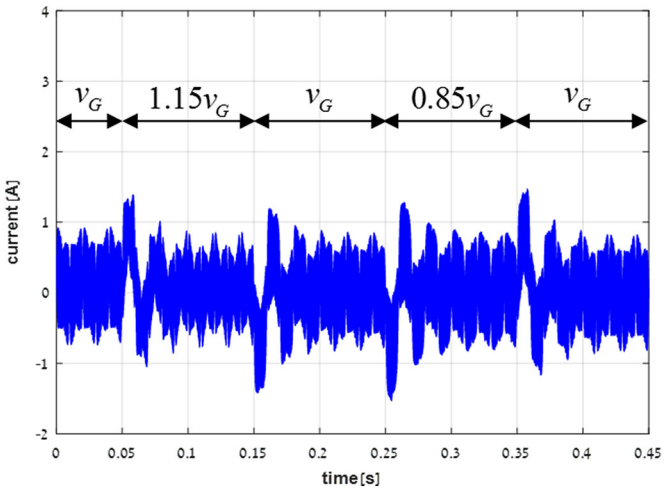

Fig. 11. Simulation results. Modified DOB-based system response to step-like grid voltage variations.

be concluded that the system is quickly stabilized after step jumps of the grid voltage.

B. Experiments

In order to experimentally validate the performance of the proposed modified filter-based DOB, a low-voltage prototype of the system was built and tested, based on modified Texas Instruments High-Voltage Single-Phase Inverter Development Kit. The experimental setup is depicted in Fig. 12. During experiments, dc and grid voltage values were scaled down by factor of 8 compared to simulations (cf. Table III), while the parameters in Tables I and II remained unchanged. The control system was implemented digitally using Concerto F28M35 control card.

The converter was connected to a distorted grid after synchronization sequence.

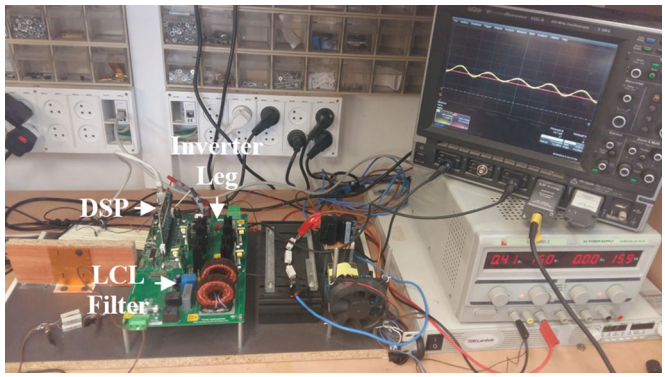

Fig. 12. Experimental setup.

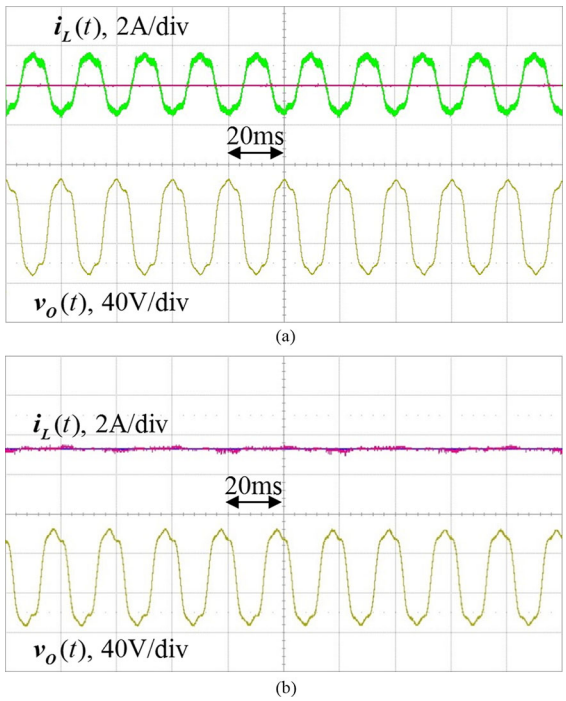

Fig. 13. Experimental results: grid voltage and inductor current. (a) With original DOB. (b) With modified DOB.

Experimental waveforms corresponding to simulation ones are shown in Figs. 13 and 14. Obviously, experimental results closely match simulation outcomes, verifying excellent performance of DOB with the modified filter and its superiority over the original one. The LUD along with its modified-filter-based DOB estimate nearly overlap, as shown in Fig. 15, enlightening the reason for outstanding performance demonstrated by the observer based on the proposed modified filter.

In the second experiment, nominal controller output u_n was generated by a proportional-resonant tracking controller [39]

$$C_n(s) = \frac{(Ls + R)\left(2\omega_C s + \omega_C^2\right)}{s^2 + \omega_0^2} \tag{44}$$

with $\omega_C = 1000\pi$ rad/s and

$$i_L^*(t) = 3\sin\omega_0 t \ \ (\mathrm{A}) \tag{45}$$

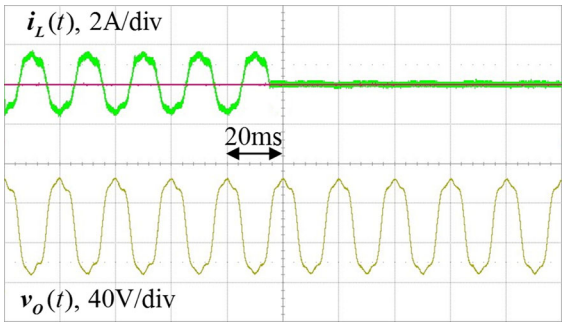

Fig. 14. Experimental results. Classical-to-modified DOB-based operation transition.

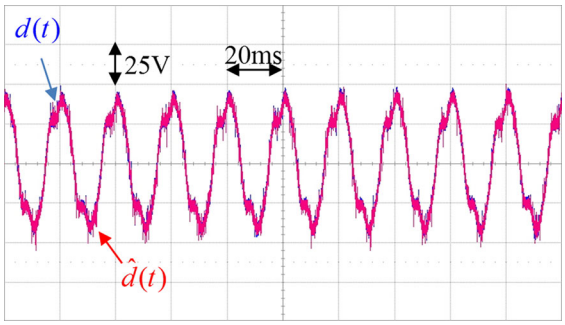

Fig. 15. Experimental results. LUD and its modified-filter-based DOB estimate.

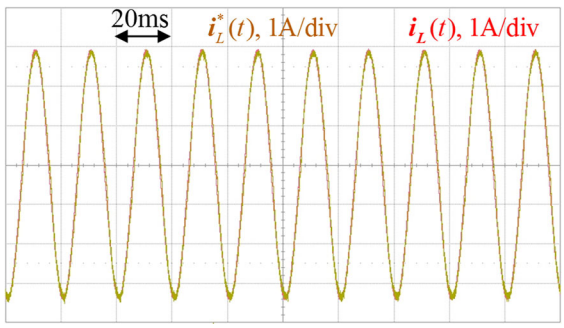

Fig. 16. Experimental results. Tracking a sinusoidal reference.

describing the inductor current reference signal. The result is shown in Fig. 16. Accurate tracking is evident, again demonstrating great disturbance rejection capabilities of the proposed control structure.

VII. Conclusion

In this paper, the methodology for modifying DOB filters in order to enhance the capability of coping with periodic uncertainties and disturbances was introduced. Owing to an additional multiresonant term, the modified filter possesses unity gain and zero phase at dc and base frequency multiples, granting the system improved ability of periodic uncertainties and disturbances rejection. Following the additional multiresonant term analysis, design guidelines were given and possible trade-offs were discussed. The revealed findings were successfully verified by simulations and experiments.

References

[1] W.-H. Chen, K. Ohnishi, and L. Guo, "Advances in disturbance/uncertainty estimation and attenuation," *IEEE Trans. Ind. Electron.*, vol. 62, no. 9, pp. 5758–5762, Sep. 2015.
[2] J. Yang, W.-H. Chen, and Z. Ding, "Disturbance observers and applications," *Trans. Inst. Meas. Control*, vol. 38, no. 6, pp. 621–624, 2016.
[3] W.-H. Chen, J. Yang, L. Guo, and S. Li, "Disturbance-observer-based control and related methods—An overview," *IEEE Trans. Ind. Electron.*, vol. 63, no. 2, pp. 1083–1095, Feb. 2016.
[4] S. Li, J. Wei, K. Guo, and W.-L. Zhu, "Nonlinear robust prediction control of hybrid active-passive heave compensator with extended disturbance observer," *IEEE Trans. Ind. Electron.*, vol. 64, no. 8, pp. 6684–6694, Aug. 2017.
[5] R. Cui, L. Chen, C. Yang, and M. Chen, "Extended state observer based integral sliding mode control of an underwater robot with unknown disturbances and uncertain nonlinearities," *IEEE Trans. Ind. Electron.*, vol. 64, no. 8, pp. 6785–6795, Aug. 2017.
[6] L. Sun and Z. Zheng, "Disturbance observer based robust backstepping altitude stabilization of spacecraft under input saturation and measurement uncertainty," *IEEE Trans. Ind. Electron.*, vol. 64, no. 10, pp. 7994–8002, Oct. 2017, doi: 10.1109/TIE.2017.2694349.
[7] H. An, J. Liu, C. Wang, and L. Wu, "Disturbance observer based anti-windup control for air-breathing hypersonic vehicles," *IEEE Trans. Ind. Electron.*, vol. 63, no. 5, pp. 3038–3049, May 2016.
[8] J. Karttunen, S. Kallio, P. Peltoniemi, and P. Silventoinen, "Current harmonic compensation in dual three-phase PMSMs using a disturbance observer," *IEEE Trans. Ind. Electron.*, vol. 63, no. 1, pp. 583–594, Jan. 2016.
[9] X. Li, S.-L. Chen, C. S. Teo, and K. K. Tan, "Data-based tuning of reduced order inverse model in both disturbance observer and feedforward with application to tray indexing," *IEEE Trans. Ind. Electron.*, vol. 64, no. 7, pp. 5492–5501, Jul. 2017.
[10] M. Sitbon, S. Schacham, and A. Kuperman, "Disturbance observer based voltage regulation of current mode boost converter interfaced photovoltaic generator," *IEEE Trans. Ind. Electron.*, vol. 62, no. 9, pp. 5776–5785, Sep. 2015.
[11] K. Ohishi, M. Nakao, K. Ohnishi, and K. Miyachi, "Microprocessor controlled dc motor for load-insensitive position servo system," *IEEE Trans. Ind. Electron.*, vol. 34, no. 1, pp. 44–49, Feb. 1987.
[12] A. Kuperman, Y. Horen, and S. Tapuchi, "Input-output nominalization of linear plants with slow varying uncertainties," *Int. J. Comp. Math. Electr. Electron. Eng.*, vol. 29, no. 1, pp. 72–89, 2010.
[13] K.-J. Lee, B.-G. Park, R.-Y. Kim, and D.-S. Hyun, "Robust predictive current controller based on a disturbance estimator in a three-phase grid-connected inverter," *IEEE Trans. Power Electron.*, vol. 27, no. 1, pp. 276–283, Jan. 2012.
[14] J. Ren, Y. Ye, G. Xu, Q. Zhao, and M. Zhu, "Uncertainty and disturbance estimator based control scheme for PMSM drives with a simple parameter tuning," *IEEE Trans. Power Electron.*, vol. 32, no. 7, pp. 5712–5722, Jul. 2017, doi: 10.1109/TPEL.2016.2607228.
[15] X. Zhang, B. Hou, and Y. Mei, "Deadbeat predictive current control of permanent magnet synchronous motors with stator current and disturbance observer," *IEEE Trans. Power Electron.*, vol. 32, no. 5, pp. 3818–3834, May 2017, doi: 10.1109/TPEL.2016.2592534.
[16] E. Sariyildiz and K. Ohnishi, "Stability and robustness of disturbance-observer-based motion control systems," *IEEE Trans. Ind. Electron.*, vol. 62, no. 1. pp. 414–422, Jan. 2015.
[17] M. Roes, J. Duarte, and M. Hendrix, "Disturbance observer based control of a dual output LLC converter for solid state lightning applications," *IEEE Trans. Power Electron.*, vol. 26, no. 7, pp. 2018–2027, Jul. 2011.
[18] C. Wang, X. Li, L. Guo, and Y. W. Li, "A nonlinear disturbance observer based DC bus voltage control for a hybrid AC/DC microgrid," *IEEE Trans. Power Electron.*, vol. 29, no. 11, pp. 6162–6177, Nov. 2014.
[19] M. Ruderman, A. Ruderman, and T. Bertram, "Observer-based compensation of additive periodic torque disturbances in permanent magnet motors," *IEEE Trans. Ind. Inf.*, vol. 9, no. 2, pp. 1130–1138, May 2013.
[20] H. Chu, B. Gao, W. Gu, and H. Chen, "Low-speed control for permanent-magnet dc torque motor using observer-based nonlinear triple-step controller," *IEEE Trans. Ind. Electron.*, vol. 64, no. 4, pp. 3286–3296, Apr. 2017.
[21] W. H. Chen, "Harmonic disturbance observer for nonlinear systems," *J. Dyn. Syst. Meas. Control*, vol. 125, no. 1, pp. 114–117, 2003.
[22] W. H. Chen, "Disturbance observer based control for nonlinear systems," *IEEE/ASME Trans. Mechatron.*, vol. 9, no. 4, pp. 706–710, Dec. 2004.
[23] E. Sariyildiz and K. Ohnishi, "A guide to design disturbance observer," *J. Dyn. Syst. Meas. Control*, vol. 136, no. 2, pp. 11–20, Dec. 2013.

[24] Y. Choi, K. Yang, W. K. Chung, H. R. Kim, and I. H. Suh, "On the robustness and performance of disturbance observers for second-order systems," *IEEE Trans. Autom. Control*, vol. 48, no. 2, pp. 315–320, Feb. 2003.

[25] N. H. Jo, C. Jeon, and H. Shim, "Noise reduction disturbance observer for disturbance attenuation and noise suppression," *IEEE Trans. Ind. Electron.*, vol. 64, no. 2, pp. 1381–1391, Feb. 2017.

[26] Y. Joo, G. Park, J. Back, and H. Shim, "Embedding internal model in disturbance observer with robust stability," *IEEE Trans. Autom. Control*, vol. 61, no. 10, pp. 3128–3133, Oct. 2016.

[27] M. Mellincovsky, V. Yuhimenko, M. M. Peretz, and A. Kuperman, "Low-frequency DC link ripple elimination in power converters with reduced capacitance by multiresonant direct voltage regulation," *IEEE Trans. Ind. Electron.*, vol. 64, no. 3, pp. 2015–2023, Mar. 2017.

[28] L. F. A. Pereira, J. V. Flores, G. Bonan, D. F. Coutinho, and J. M. G. da Silva, Jr., "Multiple resonant controllers for uninterruptible power supplies—A systematic robust control design approach," *IEEE Trans. Ind. Electron.*, vol. 61, no. 3, pp. 1528–1538, Mar. 2014.

[29] M. Castilla, J. Miret, J. Matas, L. Garcia de Vicuna, and J. Guerrero, "Linear current control scheme with series resonant harmonic compensator for single phase grid connected photovoltaic inverters," *IEEE Trans. Ind. Electron.*, vol. 55, no. 7, pp. 2724–2733, Jul. 2008.

[30] M. Castilla, J. Miret, J. Matas, L. Garcia de Vicuna, and J. Guerrero, "Control design guidelines for single-phase grid-connected photovoltaic inverters with damped resonant harmonic compensators," *IEEE Trans. Ind. Electron.*, vol. 56, no. 11, pp. 4492–4501, Nov. 2009.

[31] M. Castilla, J. Miret, A. Camacho, J. Matas, and L. Garcia de Vicuna, "Reduction of current harmonic distortion in three phase grid connected photovoltaic inverters via resonant current control," *IEEE Trans. Ind. Electron.*, vol. 60, no. 4, pp. 1464–1472, Apr. 2013.

[32] M. Sitbon, S. Schacham, and A. Kuperman, "Disturbance observer based voltage regulation of current-mode-boost-converter-interfaced photovoltaic generator," *IEEE Trans. Ind. Electron.*, vol. 62, no. 9, pp. 5776–5785, Sep. 2015.

[33] Y. Mohamed and E. El-Saadany, "A robust natural-frame-based interfacing scheme for grid-connected distributed generation inverters," *IEEE Trans. Energy Convers.*, vol. 20, no. 3, pp. 728–736, Sep. 2011.

[34] J. Kukkola, M. Hinkkanen, and K. Zenger, "Observer-based state-space current controller for a grid converter equipped with and LCL filter: Analytical method for direct discrete-time design," *IEEE Trans. Ind. Appl.*, vol. 51, no. 5, pp. 4079–4090, Sep. 2015.

[35] J. Kukkola and M. Hinkkanen, "State observer for grid voltage sensorless control of a converter equipped with and LCL filter: Direct discrete-time design," *IEEE Trans. Ind. Appl.*, vol. 52, no. 4, pp. 3133–3145, Jul. 2016.

[36] A. Rahoui, A. Bechouche, H. Seddiki, and D. Abdeslam, "Grid voltages estimation for three-phase PWM rectifiers control without AC voltage sensors," *IEEE Trans. Power Electron.*, vol. 33, no. 1, pp. 859–875, Jan. 2018.

[37] Q.-C. Zhong, A. Kuperman, and R. Stobart, "Design of UDE-based controllers from their two-degree-of-freedom nature," *Int. J. Nonlinear Robust Control*, vol. 21, no. 17, pp. 1994–2008, 2011.

[38] D. G. Holmes, T. A. Lipo, B. P. McGrath, and W. Y. Kong, "Optimized design of stationary frame three phase AC current regulators," *IEEE Trans. Power Electron.*, vol. 24, no. 11, pp. 2417–2426, Nov. 2009.

[39] A. Kuperman, "Proportional-resonant current controllers design based on desired transient performance," *IEEE Trans. Power Electron.*, vol. 30, no. 10, pp. 5341–5345, Oct. 2015.

Authors' photographs and biographies not available at the time of publication.